Multiscale mechanical design of the lightweight, stiff, and damage-tolerant cuttlebone: a computational study

Edward Lee, Zian Jia, Ting Yang, Ling Li

Department of Mechanical Engineering, Virginia Polytechnic Institute and State University, 635 Prices Fork Rd, VA 24060, USA

Corresponding Author: Ling Li

ABSTRACT: Cuttlebone, the endoskeleton of cuttlefish, offers an intriguing biological structural model for designing low-density cellular ceramics with high stiffness and damage tolerance. Cuttlebone is highly porous (porosity ~93%) and lightweight (density less than 20% of seawater), constructed mainly by brittle aragonite (95 wt%), but capable of sustaining hydrostatic water pressures over 20 atmospheres and exhibits energy dissipation capability under compression comparable to many metallic foams (~4.4 kJ/kg). Here we computationally investigate how such a remarkable mechanical efficiency is enabled by the multiscale structure of cuttlebone. Using the common cuttlefish, *Sepia Officinalis*, as a model system, we first conducted high-resolution synchrotron micro-computed tomography (μ-CT) and quantified the cuttlebone's multiscale geometry, including the 3D asymmetric shape of individual walls, the wall assembly patterns, and the long-range structural gradient of walls across the entire cuttlebone (*ca.* 40 chambers). The acquired 3D structural information enables systematic finite-element simulations, which further reveal the multiscale mechanical design of cuttlebone: at the wall level, wall asymmetry provides optimized energy dissipation while maintaining high structural stiffness; at the chamber level, variation of walls (number, pattern, and waviness amplitude) contributes to progressive damage; at the entire skeletal level, the gradient of chamber heights tailors the local mechanical anisotropy of the cuttlebone for reduced stress concentration. Our results provide integrated insights into understanding the cuttlebone's multiscale mechanical design and provide useful knowledge for the designs of lightweight cellular ceramics.

KEYWORDS: Biomechanics, cuttlebone, multiscale mechanical design, energy absorption, lightweight cellular materials, multifunctionality.

1. Introduction

The cuttlefish, which belong to the class Cephalopoda (also includes octopus or squid), are mollusks that are capable of swimming. Unlike fishes that use inflatable swim bladders to control their buoyancy, the cuttlefish utilizes a hard, internal skeletal structure known as cuttlebone to achieve this purpose [1] (**Fig. 1a**). The cuttlefish adjusts its buoyancy by controlling the in- and outflow of water in cuttlebone by changing the salt concentrations of the fluid inside through an osmotic process [2–4].To achieve this biological function, cuttlebone has developed a highly porous structure (porosity ~ 93%). It is mainly made of aragonite (~95 wt%), a crystal form of calcium carbonate, which allows cuttlefish such as *Sepia Officinalis* (one of the largest common cuttlefish) to adjust its buoyancy and swim down to 200 m underwater (with an equivalent water pressure of ~2 MPa), meanwhile other *Sepia* species may survive in estimated depths even greater than 600 m underwater [5,6].

The cuttlebone can withstand strong underwater pressures, prevent implosion (specific strength >680 N·m/kg), and possess high specific energy dissipation (~4.4 kJ/kg) comparable to many metallic foams [7]. Considering that the strength of cuttlebone is only 1/200 of steel, this high specific energy dissipation is extremely impressive. Moreover, as cuttlebone is composed mainly of brittle calcium carbonate (aragonite as the crystal phase), its hierarchical material architecture is expected to be the major contributor to cuttlebone's impressive mechanical performance, which underlies the motivation to study how cuttlebone is structured at multiple length scales.

It has been shown that the cuttlebone consists of a unique interior cellular structure covered by an exterior dorsal shield (**Fig. 1b, e**) [5]. Like many other chambered cephalopod shells [8,9], the cuttlebone's cellular structure consists of multiple chambered layers partitioned by septa, and each chamber is supported by uniquely designed pillar-like walls **(Fig. 1c**) [10]. Early studies have examined the morphometrics of the cuttlebone structure of a variety of cuttlefish; it was found that differences in species of the cuttlefish and feeding patterns have effects on the overall shape of the cuttlebone [11], though all shared the same corrugated wall-septa design. The constituent properties of cuttlebone had been characterized by North et al., who utilized nanoindentation to show that the outer side of the dorsal shield exhibits an elastic modulus of about 63.0 GPa whereas the modulus of pillars and septa (**Fig. 1c, e**) are about 51.0 and 30.0 GPa, respectively. Gower et al. further revealed that the cuttlebone displayed progressive damage under compression, exhibiting chamber by chamber failure [10]. More recently, Yang et al. have demonstrated that the specific stiffness of cuttlebone is over three times that of the octet truss, close to that of the mechanical metamaterials that have stiffness approaching the theoretical limit [7,12]. From the results of in-situ compression tests, nanoindentation, and computer simulations, it was further

demonstrated that the wavy and corrugated walls of cuttlebone are helpful to constrain damages to well-defined locations (middle portion of the walls) and thus enhance the energy absorption capability of cuttlebone by a more extensive densification process [7].

The stiff, lightweight, high energy absorption properties of cuttlebone are highly desired in practical materials such as engineering ceramic foams and architected lattice materials [7,13]. Topology optimization has been conducted on cuttlebone-inspired models to investigate the effect of porosity, where it was found that optimal performance is achieved at around 82.5% porosity, relatively similar to that of the cuttlebone [14]. Researchers have also tried to mimic the geometry of cuttlebone using additive manufacturing [5,13–15], and recently, Mao et al. have designed cuttlebone-inspired lattices to achieve specific strength and energy absorption around 20 and 25 times those of polymer foams [16]. These previous studies have established significant knowledge on the mechanics of cuttlebone and bio-inspired applications of cuttlebone [7,10,15,16], however, 1) the multiscale mechanics of cuttlebone has not been understood comprehensively and 2) most previous studies are based on fixed wall geometries arranged periodically, the diverse, wavy, and nonperiodic arrangement of walls at different chambers across the cuttlebone has not yet been studied.

To improve the cuttlebone-inspired designs, it is necessary to delineate the multiscale characteristics of the cuttlebone and investigate their effects on the mechanical performance of the structure more systematically; the structure shall be observed on the single wall, chamber, and skeletal levels. Moreover, it remains elusive how the large-scale structural variation of walls and chambers in the cuttlebone affect the integrity and biological function of the cuttlebone. Further quantification of the multiscale structure-property relation of cuttlebone may provide constructive insights into cuttlebone-inspired designs.

In this study, we first unveil the geometric features of the cuttlebone structure quantitatively through μ-CT based analysis, particularly focusing on the geometrical variations of walls across the entire cuttlebone. The 3D geometric information is used to generate the finite-element models of single walls and chambers at different locations of the cuttlebone. We then investigate how the mechanical performance of the cuttlebone is controlled by its hierarchical geometry, including the design of individual walls, chambers, and the structural gradient across the entire cuttlebone. The mechanical principles found in this study may inspire the design of lightweight, high-temperature resistant, and mechanical robust cellular ceramics, having potential applications in packing, transportation, and infrastructure.

2. Experimental and computational methods

2.1. Sample preparation and SEM imaging

The cuttlebone samples were dissected from frozen adult cuttlefish *S. officinalis* and air-dried at room temperature before imaging. The cuttlebone samples were fractured perpendicular to the dorsal-ventral direction. The fractured sections were mounted on scanning electron microscope (SEM) stubs and coated with ~8 nm Pt/Pd with a sputter coater (Leica Double Sputter Coater). The samples were then imaged using a Quanta 600 FEG Environmental SEM (FEI, OR). SEM images were taken at an accelerating voltage of 5 kV and a working distance of ~10 mm.

2.2. Synchrotron μ-CT measurement

The synchrotron μ-CT measurements were conducted at beamline 2BM of the Advanced Photon Source (APS), Argonne National Laboratory (ANL). A schematic of the experiment setup is shown in Fig. S1, where a monochromatic X-ray beam with an energy of 27.4 keV was used. For each tomography scan, the sample was rotated by 180 degrees, and 1500 projections were obtained. The projection images were collected by using a PCO-Edge high-speed CMOS detector (2448 × 2448 pixels) with a voxel size of $1.725^3\ \mu m^3$. The exposure time for each projection was 0.035s. The collected projection data were then reconstructed using Tomopy [16]. 11 reconstruction data sets were collected and stitched together using Fiji/ImageJ [17] to obtain a single continuous 3D dataset of the rectangular block of cuttlebone, as depicted by the white box of **Fig. 1b**. The reconstructed data was further segmented using Avizo (Thermo Fisher Scientific, MA, USA) to produce 3D models of the cuttlebone (**Fig. 1e**).

2.3 Wall curvature and spacing analysis

The curvature analysis of individual walls reconstructed from the μ-CT data was conducted in Avizo. The principal curvatures, including the minimum curvature κ_1 and the maximum curvature κ_2, at individual nodes on the triangular surface meshes of cuttlebone walls were calculated as follows. First, each quadratic surface was fitted to the node of interest and three layers of its surrounding neighboring nodes. Then, the initial principal curvatures were calculated from the eigenvalues and eigenvectors of the Hessian matrix for the fitted quadratic surface. Finally, the initial principal curvature values for the node of interest were averaged four times with the curvature values of the surrounding neighboring nodes. The interfacial shape distribution of the calculated principal curvatures κ_1 and κ_2 was plotted in OriginPro 2016 (OriginLab. MA, USA). The mean curvature, κ_{mean}, and Gaussian curvature, κ_G, were then calculated as $\kappa_{mean} = (\kappa_1+\kappa_2)/2$ and $\kappa_G = \kappa_1 \cdot \kappa_2$, respectively.

The spacing between adjacent walls within individual chambers was measured using the thickness map module in Avizo. The segmented wall pattern in each chamber was first skeletonized in Fiji/ImageJ [17] and converted to walls of one-pixel thickness. The thickness map module then computes the spacing between the adjacent skeletonized wall pattern. Specifically, the spacing is quantified as the diameter of the largest sphere that can be fitted into two adjacent walls [18].

2.4. FEM analysis methods

The 3D models used in FEM analysis were based on the synchrotron μ-CT data. Using slices of the segmented data, the profiles of cuttlebone walls and chambers can be extracted as depicted in Fig. S1. This stack of slice data was further transferred to Solidworks (Dassault Systèmes, France) using a customized MATLAB (MathWorks, America) program to construct 3D geometric models of cuttlebone walls and chambers. The resultant geometries were then imported into ABAQUS (Dassault Systèmes, France) for meshing and FEM simulations. From the simulations, the resulting stress, σ, and strains, ε, can be obtained. The walls and septa of the cuttlebone were represented by shell and tetrahedral elements, and with Young's moduli, E, of 51 GPa and 29.6 GPa, respectively [19]. The Poisson's ratio was set as 0.4 for both the walls and the septa.

The elastic response was computed with general statics and the fracture process was simulated by the dynamic explicit module; the strain rate of loading was set as 0.05/s for the explicit simulations. Due to the brittle nature of the biogenic aragonite composing the cuttlebone walls, a brittle cracking model and element deletion were implemented. Note that the cuttlebone structure fails via strength-controlled fracture, not by buckling, as previous studies have shown that increasing the wall waviness (second moment of area) resulted in lower stress of failure [7]. More specifically, cracks initiate in the walls when the maximum principal stresses exceeded the tensile strength of aragonite, which was set as 102 MPa in the simulation [20]. To avert an irrational mesh sensitivity, the criteria for element deletion was defined by the fracture energy of forming a unit area of crack surface on Mode I, G_{If} [21]. A material point is considered to fail when the critical fracture energy (G_{If}) is reached. An element is considered to fail and deleted when all the corresponding material points of this element fail. Also note that a linear shear retention model was included to model the reduction of post-cracked shear modulus once the crack has opened [7].

For the single wall simulations, uniaxial compression (compressed along the wall height direction) is conducted. The walls are fixed on the top and bottom edges to represent the strong wall-septa connections. A compressive displacement is further applied along the top edge of the walls to mimic the deformation induced in the cuttlebone when it is under water pressure. At the chamber level, compression and shear in different directions are simulated. Finally, at the entire cross-section level, the simulation is based on a 2D model, where the dorsal shield and soft tissue were integrated. Note that the material properties of the soft tissue are based on the literature and

a hyperelastic Arruda-Boyce model is adopted with a shear modulus (μ) of 27.5 kPa, locking deformation or stretch (λ_m) of 1.17, and compressibility (D) of 0.004 kPa^{-1} [22,23].

3. Results and Discussion

3.1. Overview of cuttlebone structure

As shown in **Fig. 1a**, the cuttlebone (highlighted in yellow) is located on the dorsal side of the cuttlefish; the anterior (head of the cuttlefish) and posterior (tail of the cuttlefish) directions are also illustrated in this figure. **Fig. 1b** shows a cross-sectional view of the cuttlebone, from which individual chambered layers can be observed. In addition, a thick, mineralized shell is present on the dorsal side of the cuttlebone, known as the dorsal shield. In this study, a sample section was isolated from the *S. Officinalis* cuttlebone shown in **Fig. 1b** to investigate the morphological variation of the chambered structure across the dorsal-ventral direction. **Fig. 1c** and **e** reveal that these chambers consist of "pillar-like meandering walls" separated by septa [10]. A representative synchrotron-based μ-CT reconstruction slice in **Fig. 1d** clearly shows the individual layered chambers supported by vertical walls. This inspected cuttlebone volume consists of 38 chambers in total, which are labeled as C1, C2, …, and C38 from the ventral to the dorsal side (**Fig. 1d**). The heights of these chambers exhibit a gradual increase from C1 (140 μm) to C20 (500 μm) and remains relatively constant towards C38, as shown in **Fig. 1f**. The variation of chamber height for the entire cuttlebone cross-section is shown in **Fig. 1b**.

3.2. The asymmetric wall morphology

Previous work has shown the vertical walls in cuttlebone are corrugated and exhibits a characteristic waviness gradient [7]. **Fig. 2a** shows a representative wall isolated from Chamber 22, from which we can see that the cross-sectional profile of the wall becomes wavier toward the ventral side. Here h is the height position of the cross-section and h_0 is total wall height (see the inset schematic in **Fig. 2b**). To further characterize the waviness of the walls across the entire cuttlebone systematically, the normalized cross-sectional lengths ($\frac{L}{L_{dorsal}}$) of representative walls acquired from different chambers (W4, W8, W14, W18, W22, W29, and W36) are measured as functions of the normalized wall height ($\frac{h}{h_0}$) (**Fig. 2b**). The definition of wall length is depicted in the inset of **Fig. 2b**, where L_{ventral} and L_{dorsal} represent the wall's cross-sectional lengths at the ventral and dorsal sides, respectively. L represents the cross-sectional wall length at height h. **Fig. 2b** clearly shows that $\frac{L}{L_{dorsal}}$ increases from the dorsal to ventral side for all the walls in different chambers, indicating a directional asymmetric wall waviness. We further fit the profile to an

exponential profile $\frac{L}{L_{dorsal}} = a + (1-a)e^{c\frac{h}{h_0}}$, where a and c are calculated fitting parameters. The length ratio $\frac{L_{ventral}}{L_{dorsal}}$ (wavy side: straight side) is used as a measure of the wall waviness. The fitting results for the seven walls at different locations of the cuttlebone are summarized in Table S1.

To characterize the morphological variations of individual walls, we also plot the distribution of mean curvature (κ_{mean}) and the corresponding interfacial shape distribution of the principal curvatures κ_1 and κ_2 in **Fig. 2c** and **d**, respectively. From the distribution of principal curvatures (κ_1 and κ_2) in the interfacial shape distribution plots (**Fig. 2d**), it is discovered that the principal curvatures of all seven walls lie in the second quadrant, i.e., the Gauss curvature ($\kappa_G = \kappa_1\kappa_2$) of these walls are negative, demonstrating that the walls are "saddle-shaped". Moreover, all the data points in **Fig. 2d** sit near the axes, where one of the principal curvatures is close to zero, this result further reflects the columnar-like shape of the wall along the height direction. Therefore, the walls of the cuttlebone exhibit a characteristic columnar-like morphology and their entire surfaces are "saddle-shaped".

Within each chamber, the arrangement of walls, i.e., the labyrinthine pattern, is more aligned (along the anterior-posterior direction) in the posterior region than that in the anterior region (Fig. S2a). Such alignment is presumably tailored for more efficient fluid flow in the siphonal zone at the posterior end [3]. The same pattern variation is also observed at different chambers along the ventral-dorsal direction, as shown by five selected chambers (C4, C8, C14, C22, and C36), where it is seen that the walls are less aligned from the ventral to the dorsal side of the animal (Fig. S2b**)**. Moreover, the variations in the spacing of adjacent walls for all analyzed chambers are not significant (Fig. S2c). However, within each chamber, the spacing of the wall tops is considerably smaller than that of wall bottoms (60 μm vs.90 μm), as summarized in Table S2. It is also observed that generally, the wall heights are larger towards the dorsal side of the cuttlebone (**Fig. 1b, d, f**). Furthermore, examining the profile of the walls (**Fig. 2b** and Table S3), it is discovered that the waviness ratio of the wall is smaller in the middle chambers as opposed to that of the walls from the dorsal or ventral sides. Additional characterization of the walls is done and plotted via normalized length versus normalized height (Fig. S3).

3.3. Mechanics of a single wall

With the 3D reconstructed geometries of the seven representative single walls extracted from different chambers, stress distribution and fracture behavior of the walls under compression were simulated (**Fig. 3a**). Based on the simulation, the force-displacement curves (**Fig. 3b**) and specific

wall stiffnesses (**Fig. 3c**) were obtained. The majority of the walls fail at an applied displacement of approximately 1 μm to 2.5 μm with resulting compressive forces of 0.2 N to 0.4 N except for the shortest wall, Wall 4, which exhibits a failure force of ~ 0.7 N. Moreover, all the walls exhibit a similar failure strain of 0.0025 to 0.005 and fail at maximum principal stress of around 100 MPa (Fig. S4). Notably, the stiffness of the walls decreases drastically in walls from chambers on the ventral side towards walls from chambers on the dorsal side (**Fig. 3c**). By correlating wall height with wall stiffness and strength, it is found that shorter walls typically have higher stiffness and strength, while no strong correlation is identified between the failure displacement and wall height (**Fig. 3d**). Therefore, the variation of wall height at different locations of the cuttlebone produces material property gradients of stiffness and strength.

Simulations were further performed on three sets of artificially generated walls with controlled waviness variations to reveal the effects of the waviness on the stiffness, strength, and energy dissipation of the walls. The methods of generating these wall morphologies have been described in [7]. Specifically, the waviness of these walls is controlled to vary on a normalized scale as depicted in **Fig. 4d** (with normalized waviness A = 1.0 being the original waviness of the wall in the cuttlebone) [7]. Through compressive fracture simulations depicted in the methods section, the stiffness, strength, and energy dissipation of these walls can be retrieved (**Fig. 4a-c**).

It is observed that there exist tradeoffs between the allowable force before failure and the acceptable strain of the walls. A larger waviness amplitude yields a larger allowable strain but a lower force at failure and vice versa. An optimal waviness of energy dissipation is observed for all the three walls simulated. Interestingly, the optimal value of A is close to 1 but not always equal to 1, suggesting that the morphology of the cuttlebone has achieved an optimal waviness amplitude only "on average" in a statistical sense (**Fig. 4a-c**). A better understanding of this statistical optimization of single walls requires investigations of the mechanics of the cuttlebone chambers.

3.4. Mechanics of the cuttlebone under compression

Aside from analyzing the mechanics of individual walls, simulations were further performed on cuttlebone chambers with various wall heights under compression (**Fig. 5**). The calculated stress distributions of three selected chambers 4, 22, and 36 at an applied strain of 0.001 are depicted in **Fig. 5a-c.** It is seen that the walls endure maximum principal stress in the middle portion where initiation of fracture takes place most often, which is consistent with our single-wall simulations (**Fig. 3**) and previous synchrotron-based *in-situ* measurements [7].

The profiles of walls present in the three chambers are characterized in **Fig. 5d**, where the number of walls in the corresponding chamber is labeled as "n". It is observed that chambers located towards the ventral side (with shorter walls) exhibit a higher number of walls per unit area.

A comparison of the stress-strain response of the three chambers (also compared to literature results [7]) is shown in **Fig. 5e**. Although all chambers exhibit graceful failure, it is revealed that the number of walls in each chamber correlates positively with the failure strain (the level of progressive failure) of the chamber (**Fig. 5f**).

At the single wall level, we demonstrated that wavier walls typically promote a more progressive damage behavior (**Fig. 4**). Here, as seen in **Fig. 5**, however, chamber 4, which exhibits the least wavy walls in comparison to those in chambers 22 and 36, yields the greatest failure strain and thus the most progressive damage. This discrepancy at individual wall level and chamber level suggests that different factors contribute to the graceful failure at different structural levels.

The graceful failure observed at the chamber level may be related to the number and variety of walls in the chamber. As shown in **Fig. 5d** and referring to Tables S3 and S4, chamber 22, the centermost chamber of the three, inhabits the least number of walls in the chamber. On the contrary, the chamber closer to the ventral side of the cuttlebone (chamber 4) possesses a significantly greater number of walls. Considering that chamber 4 fails most progressively, it leads to the hypothesis that the "diversity" (concerning the number and the shape, **Fig. 5d**) of the walls in a chamber may be the main controller of progressive damage at the chamber level. The reasoning is the following: if all walls in a chamber are of the same shape, though the individual wall is optimized, they tend to fail in the same pattern and at the same applied displacement, which thus favors catastrophic damage. By contrast, if walls are of diverse shape, waviness, length, and connectivity, more progressive damage could be expected as different walls fail differently. One measure of wall diversity in cuttlebone is the number of walls. This deduction becomes more apparent in the correlation between the number of walls in each chamber and their corresponding strains at failure (**Fig. 5f**).

3.5 Anisotropic mechanical performance of the chamber

Further analysis is completed to understand the anisotropic mechanical performance of the chamber; the chamber is loaded under compression in three orthogonal directions: vertically and transversely along the x and y axes. The stress distribution for chambers 4, 22, and 36 are depicted in **Fig. 6a-c**. The mechanical behavior of chamber 22 under shear in different directions is further shown in **Fig. 7**, where the distribution of Tresca stress is presented. The effective Young's modulus and shear modulus calculated from these simulations are summarized in Fig. S5.

The aligned walls lead to strong mechanical anisotropy of the chamber. Notably, different chambers can exhibit very different mechanical anisotropy. For example, while chamber 4 is stiffer in the vertical direction, chambers 22 and 36 are stiffer in the transverse directions (Fig. S3 and Table S4).

Moreover, it is found that although the walls of the chamber (e.g., chamber 22) are highly aligned and exhibit strong geometric anisotropy in the x-y plane, however, the mechanical response of the chamber is nearly isotropic in the x-y plane (Fig. S6-7). That is, the mechanical anisotropy and geometrical anisotropy of the cuttlebone chambers are decoupled. This is highly beneficial in the biological design of cuttlebone, as wall alignment can be adjusted at different locations of the cuttlebone to tailor local fluid permeability with little effect on the elastic performance of the cuttlebone. The mechanism behind this decoupling can be explained as follows. The stiffness of the chamber in the z-direction is dominated by the walls while the stiffnesses in the x and y directions are controlled by the septa, which is evident from the stress distribution depicted in **Fig. 6**. As a result, the mechanical performances are nearly the same when loaded in the x and y directions, contributing to the observed transverse-isotropic elastic properties of cuttlebone at the chamber level.

In summary, the elastic properties of cuttlebone chambers are tailored mainly by varying the stiffness in traverse directions (E_{xx} and E_{yy}). Specifically, it is the number of septum layers at a specific height that controls E_{xx} and E_{yy} and thus the mechanical anisotropy. Chamber height is the knob that the cuttlebone uses to adjust the anisotropic mechanical properties. It should be noted that while the wall alignment has a negligible effect on the modulus in normal compression, it is important to the shear modulus (Fig. S5b).

3.6. Skeletal level design of the cuttlebone

It is known that the cuttlebone presents a characteristic fusiform covered by a dorsal shield and is surrounded by soft tissue on the bottom (**Fig. 8a**). Under water pressure, such a structural arrangement develops a distributed stress field that may presumably affect the structure parameters of the cuttlebone during its development process like how stress affects the microstructure development in cancellous bones [2] (**Fig. 8b**). To reveal the correlation between the cuttlebone shape, microstructure, and stress distribution, elastic simulations were conducted on the cuttlebone cross-section. We assume that the cuttlefish is subjected to an external pressure of 2.03 MPa, equivalent to water pressure at the depth of 200 meters (**Fig. 8f-g**). Three models were simulated including a full-scale cuttlebone with both its soft tissue and dorsal shield, a cuttlebone model with soft tissue but no dorsal shield, and a cuttlebone-only model with no soft tissue and dorsal shield (**Fig. 8**).

With the simulated distribution of maximum principal stress shown in **Fig. 8b** for the most realistic model (cuttlebone model with soft tissue and dorsal shield), it is clearly seen that the cuttlebone is dominantly under compression, as the tensile stress is 30 times smaller than the compressive stress. Moreover, the maximum compressive stress locates towards the ventral side of the cuttlebone. Similarly, the Tresca stress and Mises stress (**Fig. 8c-d**) are also higher on the

ventral side. The stress-concentration on the ventral side suggests damage of the cuttlebone to initiate therein under compression. Such locations of damage initiation have been observed experimentally: implosion tests show that when water pressure exceeds the strength of the cuttlebone, damage typically initiates at the ventral side [24]. Biologically, constraining damage initiation to the ventral side is beneficial to the subsequent self-healing process – the ventral side is the biologically active region where the growth of new chambers and walls takes place [25].

From the cuttlebone only model shown in **Fig. 8f-g**, it is seen that the stress distributes uniformly throughout the whole cuttlebone structure. With the addition of the soft tissue or body of the cuttlefish under the bottom edge of the cuttlebone (**Fig. 8h-i**), it is discovered that the stress is no longer distributed uniformly. Rather, the cuttlebone yields a large maximum tensile stress on the dorsal (top) side, which is comparable to the compressive stress on the ventral side (bottom) of the structure. This result can be explained by a negative bending moment inflicted upon the cuttlebone as seen by the tensile and compressive stresses on the dorsal and ventral sides of the cuttlebone, respectively. The soft tissue relieves the ventral edge of the cuttlebone from the initial compressive load, thus creating an uneven loading condition on the cuttlebone, and as a result, the ventral edge of the cuttlebone is "bent" inward.

By comparing models with (**Fig. 8a**) and without (**Fig. 8h**) the dorsal shield, it is clearly seen that the cuttlebone with a dorsal shield experiences maximum stress 46% less than that without the dorsal shield, where the dorsal shield relieves stress on the top edge of the cuttlebone. Thus, the dorsal shield functions as a structure that reduces the maximum tensile stress occurring in the cuttlebone caused by the soft tissue induced bending moment. The dorsal shield helps transfer higher compressive stresses towards the ventral region of the cuttlebone, where self-healing function is expected to be more active in the cuttlefish.

Not only does this prove that the morphology of the cuttlebone structure has grown such that protection is prioritized closer to the cuttlebone's biological inactive dorsal regions, but it also supports the conclusions drawn from the results of the mechanical performance of the different chambers of the cuttlebone. As observed in the stress distributions in the cuttlebone section of the soft tissue and dorsal shield model in **Fig. 8b-d**, the structure needs to be stronger towards the ventral side to endure the dominant compressive stresses caused by hydrostatic pressure. Supported by the same high-value regions of $1/h_0$ (h_0 is the septa spacing) (**Fig. 8e**) and high compressive stress on the dorsal side (**Fig. 8b**), it seems that cuttlebone produces chambers with smaller heights to reinforce the high-compressive stress ventral regions. In response to the higher stress, the chambers located on the ventral side of the cuttlebone are composed of shorter walls that entail an optimal wall height and waviness for more damage tolerant structures (chamber 4 in **Fig. 5**). This observation proves to be consistent with the results from the mechanical performance

of the fracture simulations (**Fig. 3**) where it was discovered that walls in chambers closer to the ventral side yielded a higher failure force, stress, and stiffness.

3.7 Multiscale mechanical design of the cuttlebone

From the above multiscale investigation of the cuttlebone, it was revealed that first, at the skeletal level of cm size, the cuttlebone possesses a peculiar fusiform covered by a dorsal shield. Of course, the hard, protective dorsal shield serves as a safeguard from external interactions (like protrusion from a predator's bite). Quite unexpectedly, we also discover that the presence of the dorsal shield shifts high compressive stress regions to the ventral side of the cuttlebone where new chambers are formed. This is presumably advantageous for self-healing of the cuttlebone after microdamage on the ventral side. Moreover, both the porosity and the orientation of the septa present structural gradients correlate with the stress distribution - this correlation helps to mitigate stress concentration and thus prevent the premature failure of cuttlebone.

Second, at the chamber level (about hundreds of micrometers), the height of the chambers varies significantly based on their locations in the cuttlebone, which controls the global distribution of porosity, stiffness, and strength of the cuttlebone at the skeletal level. In contrast to chamber height, the total length of walls in the chambers is relatively unchanged. Notably, the alignment of the walls in the chambers is shown to have a negligible effect on the compressive properties of cuttlebone (but affects shear properties). This helps decouple the control of fluid permeability and stiffness in cuttlebone chambers, i.e., the fluid transport properties of the chamber are controlled by the wall alignment while the mechanical anisotropy of the cuttlebone is tailored by the septa spacing. Furthermore, the correlative analysis between the morphology of the walls and the chamber fracture suggests that the diversity of walls in a chamber (including the number, length, and shape of the wall) contributes significantly to the progressive damage of cuttlebone under compression.

Third, at the single wall level, the walls exhibit corrugation with waviness gradients along the height direction. This gradient waviness is another important structural origin of the cuttlebone's mechanical robustness. Specifically, the waviness controls damage to the center portion of the wall, promotes progressive damage, and enhances energy dissipation. Notably, we show that the walls possess a columnar profile with a small negative Gaussian curvature. This unique feature further guarantees the walls simultaneously high stiffness and strength.

It should be noted that a chamber assembled by walls of the same shape (optimized on the individual wall level) does not directly add up to an optimal design of the chamber. One extreme example is that if all the ceramic walls are optimal but the same, they tend to fail concurrently and thus impede structure robustness. The above argument suggests that the wall level and the chamber

level design should be considered together to obtain the optimal structural design. That is, for the optimal design of the brittle walls in a cuttlebone chamber, a group of walls should be optimized instead of optimizing single walls independently. This result suggests that biological materials at different hierarchical levels are optimized not independently but concurrently through evolution [26]. More specifically, our observation aligns with the concept of group selection in evolutionary biology – a trait (structural feature) sometimes evolves because it benefits the group despite the fact that it may be deleterious to the individuals possessing it [27]. Our simulation results show that the cuttlebone walls are optimized only in a statistical manner (**Fig. 4**) supports this argument. Further investigation of the wall-chamber correlation is an interesting question for the following studies.

Finally, the high-resolution SEM images in **Fig. 9 iv** further reveal that the walls of cuttlebones are composed of ceramic fibers aligned in the height direction of the wall while the septum exhibits a plywood microstructure. These fibers have a diameter of sub-micrometer size and thus grant abundant interfaces which further facilitate the fracture resistance of the material. Importantly, such a fiber-plywood microarchitecture is beneficial to ensure a strong connection between the wall and the septa as well as to ensure the penetration resistance of the septum [28,29].

4. Conclusions

The cuttlebone is a remarkable lightweight cellular structure that prevents catastrophic damage under compression and also serves as a functional device for buoyancy control. In this study, we have investigated the multiscale design of cuttlebone and reveal that the excellent mechanical performance of cuttlebone is the outcome of a multiscale, hierarchical structural design including the porosity gradient across the whole cuttlebone, the variation of the chamber height at different locations, the diversity of the walls, the weakly saddle-shaped wall, as well as the fiber-plywood microstructure at the material level. Such an impressive multiscale structural design provides a blueprint for engineering lightweight, strong, energy dissipative, and multifunctional cellular ceramic materials.

Competing interest

The authors declare no competing financial interests.

Acknowledgment

We gratefully acknowledge funding from the Air Force Office of Scientific Research (FA9550-19-1-0033), National Science Foundation (DMR-1942865 and CMMI-1825646), and Institute for Critical Technology and Applied Science (ICTAS) at Virginia Tech for supporting this work. We thank Dr. Pavel D. Shevchenko and Dr. Francesco De Carlo for help with collecting the synchrotron-based μ-CT data and performing in-situ mechanical tests. We appreciate the support from the Department of Mechanical Engineering at Virginia Tech. This research used resources of the Advanced Photon Source, a U.S. Department of Energy (DOE) Office of Science User Facility operated for the DOE Office of Science by Argonne National Laboratory under Contract No. DE-AC02-06CH11357.

References

[1] Q.C. Artists, S. Smarts, M. Trickery, NOVA | Kings of Camouflage | Anatomy of a Cuttlefish, Public Broadcast. Serv. (2007).

[2] E.J. Denton, J.B. Gilpin-Brown, J. V. Howarth, The Osmotic Mechanism of the Cuttlebone, J. Mar. Biol. Assoc. United Kingdom. 41 (1961) 351–363. https://doi.org/10.1017/S0025315400023961.

[3] E.J. Denton, J.B. Gilpin-Brown, The Distribution of Gas and Liquid within the Cuttlebone, J. Mar. Biol. Assoc. United Kingdom. 41 (1961) 365–381. https://doi.org/10.1017/S0025315400023973.

[4] R.A. Jastrebsky, I.K. Bartol, P.S. Krueger, Turning performance in squid and cuttlefish: Unique dual-mode, muscular hydrostatic systems, J. Exp. Biol. 219 (2016) 1317–1326. https://doi.org/10.1242/jeb.126839.

[5] J. Cadman, S. Zhou, Y. Chen, Q. Li, Cuttlebone: Characterisation, Application and Development of Biomimetic Materials, J. Bionic Eng. 9 (2012) 367–376. https://doi.org/10.1016/S1672-6529(11)60132-7.

[6] K.M. Sherrard, Cuttlebone morphology limits habitat depth in eleven species of Sepia (Cephalopoda: Sepiidae), Biol. Bull. 198 (2000) 404–414. https://doi.org/10.2307/1542696.

[7] T. Yang, Z. Jia, H. Chen, Z. Deng, W. Liu, L. Chen, L. Li, Mechanical design of the highly porous cuttlebone: A bioceramic hard buoyancy tank for cuttlefish, Proc. Natl. Acad. Sci. U. S. A. 117 (2020) 23450–23459. https://doi.org/10.1073/pnas.2009531117.

[8] D.K. Jacobs, Chambered cephalopod shells, buoyancy, structure and decoupling: History and red herrings, Palaios. 11 (1996) 610–614. https://doi.org/10.2307/3515195.

[9] R. Lemanis, S. Zachow, F. Fusseis, R. Hoffmann, A new approach using high-resolution computed tomography to test the buoyant properties of chambered cephalopod shells, Paleobiology. 41 (2015) 313–329. https://doi.org/10.1017/pab.2014.17.

[10] D. Gower, J.F. V. Vincent, The Mechanical Design of the Cuttlebone and Its Bathymetric Implications, (1996).

[11] P. Neige, S. Boletzky, Morphometrics of the shell of three Sepia species (Mollusca: Cephalopoda): Intra- and interspecific variation, Zool. Beitraege. 38 (1997) 137–156.

[12] J.B. Berger, H.N.G. Wadley, R.M. McMeeking, Mechanical metamaterials at the theoretical limit of isotropic elastic stiffness, Nature. 543 (2017). https://doi.org/10.1038/nature21075.

[13] L.J. Gibson, M.F. Ashby, Cellular solids, 1989. https://doi.org/10.1016/0021-9290(89)90056-0.

[14] Z. Hu, V.K. Gadipudi, D.R. Salem, Topology Optimization of Lightweight Lattice Structural Composites Inspired by Cuttlefish Bone, Appl. Compos. Mater. 26 (2019) 15–27. https://doi.org/10.1007/s10443-018-9680-6.

[15] J. Song, Y. Wang, W. Zhou, R. Fan, B. Yu, Y. Lu, L. Li, Topology optimization-guided lattice composites and their mechanical characterizations, Compos. Part B Eng. 160 (2019) 402–411. https://doi.org/10.1016/j.compositesb.2018.12.027.

[16] A. Mao, N. Zhao, Y. Liang, H. Bai, Mechanically Efficient Cellular Materials Inspired by Cuttlebone, Adv. Mater. 33 (2021). https://doi.org/10.1002/adma.202007348.

[17] J. Schindelin, I. Arganda-Carreras, E. Frise, V. Kaynig, M. Longair, T. Pietzsch, S. Preibisch, C. Rueden, S. Saalfeld, B. Schmid, J.Y. Tinevez, D.J. White, V. Hartenstein, K. Eliceiri, P. Tomancak, A. Cardona, Fiji: An open-source platform for biological-image

analysis, Nat. Methods. 9 (2012) 676–682. https://doi.org/10.1038/nmeth.2019.
[18] T. Hildebrand, P. Rüegsegger, A new method for the model-independent assessment of thickness in three-dimensional images, J. Microsc. 185 (1997) 67–75. https://doi.org/10.1046/j.1365-2818.1997.1340694.x.
[19] L.E. North, Bioinspired Investigation via X-Ray Microtomography, (2018). https://cronfa.swan.ac.uk/Record/cronfa43706.
[20] U. Wegst, M. Ashby, No Title, Philos. Mag. (2004) 2167–2186.
[21] A. Hillerborg, M. Modéer, P. Petersson, No Title, Anal. Crack Form. Crack Growth Concr. by Means Fract. Mech. Finite Elem. 6 (1976) 773–781.
[22] E.M. Arruda, M.C. Boyce, A three-dimensional constitutive model for the large stretch behavior of rubber elastic materials, J. Mech. Phys. Solids. 41 (1993) 389–412. https://doi.org/10.1016/0022-5096(93)90013-6.
[23] R. Akhtar, M.J. Sherratt, J.K. Cruickshank, B. Derby, Characterizing the elastic properties of tissues, Mater. Today. 14 (2011) 96–105. https://doi.org/10.1016/S1369-7021(11)70059-1.
[24] S. Von Boletzky, Shell implosion depth and implosion morphologies in three species of sepia (cephalopoda) from the mediterranean sea, J. Mar. Biol. Assoc. United Kingdom. 64 (1984) 955–966. https://doi.org/10.1017/S0025315400047366.
[25] K. Tanabe, Y. Fukuda, Y. Ohtsuka, New Chamber Formation in the Cuttlefish Sepia esculenta HOYLE, Japanese J. Malacol. 44 (1985) 55–67. https://doi.org/10.18941/venusjjm.44.1_55.
[26] M.J. Buehler, Y.C. Yung, Deformation and failure of protein materials in physiologically extreme conditions and disease, Nat. Mater. 8 (2009) 175–188. https://doi.org/10.1038/nmat2387.
[27] E. Sober, Conceptual issues in evolutionary biology, 2006.
[28] F.D. Fischer, O. Kolednik, J. Predan, H. Razi, P. Fratzl, Crack driving force in twisted plywood structures, Acta Biomater. 55 (2017) 349–359. https://doi.org/10.1016/j.actbio.2017.04.007.
[29] Z. Jia, L. Wang, 3D printing of biomimetic composites with improved fracture toughness, Acta Mater. 173 (2019) 61–73. https://doi.org/10.1016/j.actamat.2019.04.052.

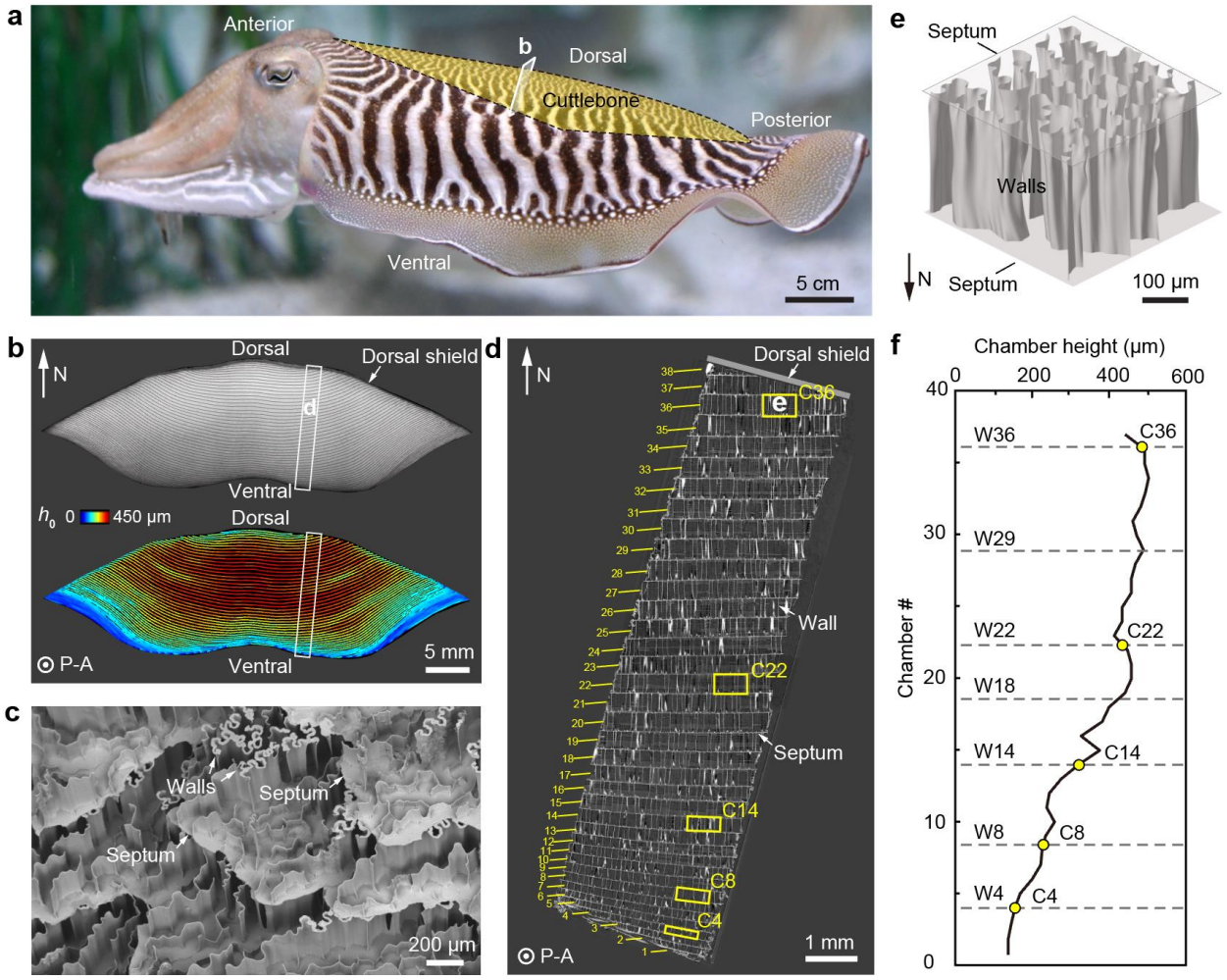

Fig. 1. The chambered structure of cuttlebone. The heterogeneous structure of cuttlebone at the wall, chamber, and structural levels. (**a**) Cuttlefish with the cuttlebone highlighted in yellow. Cuttlebone is located on the dorsal side of the cuttlefish. (**b**) Cross-section of the cuttlebone (top) and the corresponding map of chamber height (bottom). The cuttlebone sample is stripped from the rectangle labelled "d". (**c**) SEM image showing the walls and septa of the layered chambers. (**d**) Overview of the μ-CT data of the studied cuttlebone strip. The walls and chambers were numbered from the ventral side to the dorsal side. (**e**) The wall-septa structure of chamber 36 generated from the CT data. (**f**) The variation of chamber heights in the ventral to dorsal direction. The marked walls and chambers are selected for structural analysis and mechanical simulation in this study.

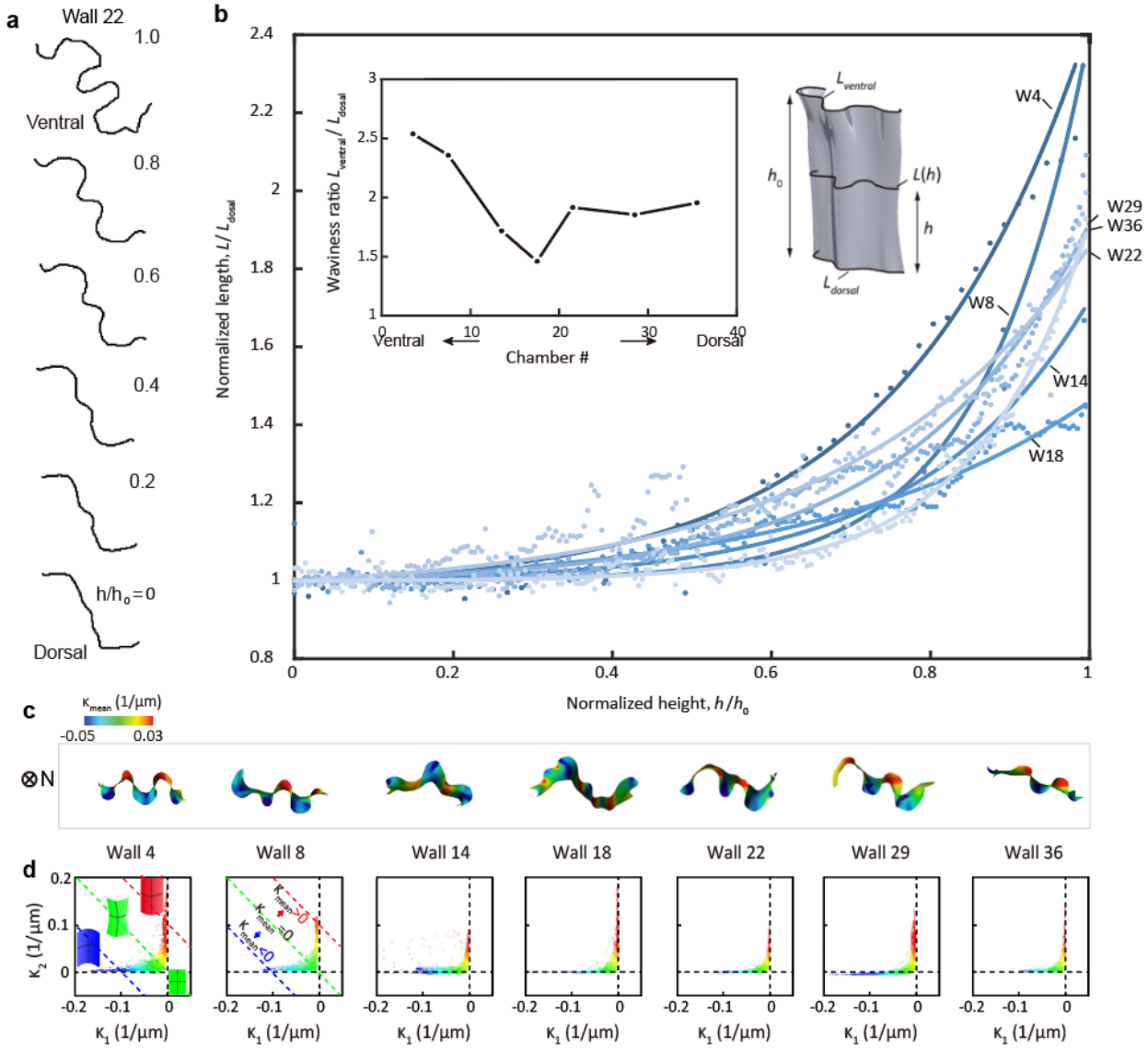

Fig. 2. Waviness analysis of seven walls with similar length at different chamber locations. (**a**) Cross-sectional profiles of wall 22 with their respective h/h$_0$ values. (**b**) The solid curves depict the fitted wall profiles in normalized form. The inset shows the length ratio $\frac{L_{ventral}}{L_{dorsal}}$ (wavy side: straight side) for the seven walls based on the chamber number. Results show that the walls are waiver at the ventral and dorsal side compared to walls in the intermediate chambers. Note that this observed trend is based on walls at different locations but share a similar length and pattern. (**c**) Ventral view of the seven walls with similar length at different chamber locations and the mean curvature (κ_{mean} = (κ_1+κ_2)/2)) of the 7 walls with location marked in Fig. 1*f*. (**d**) Principal curvature (κ_1 and κ_2) distribution of the 7 walls. The plot is colored by mean curvature the same as (**c**).

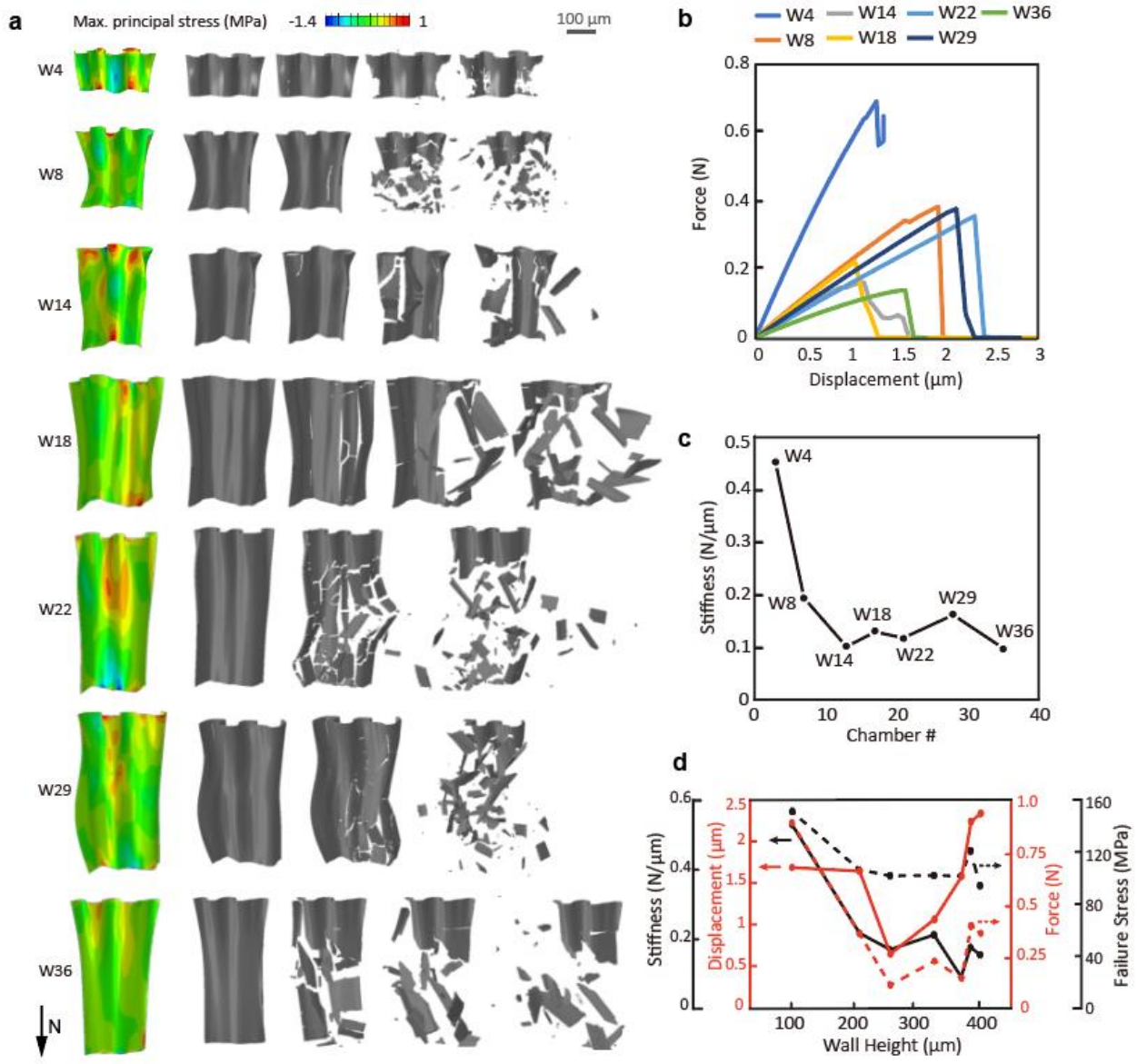

Fig. 3. Mechanical response of the seven selected walls under compression. (**a**) Stress distribution and fracture process of the selected walls under compression. (**b**) Force-displacement curves of the walls under compression. (**c**) Stiffness of the walls. (**d**) Mechanical property correlations of the seven single walls with failure displacement, force at failure, stress at failure, and stiffness plotted versus wall height based on the fracture simulation of individual walls.

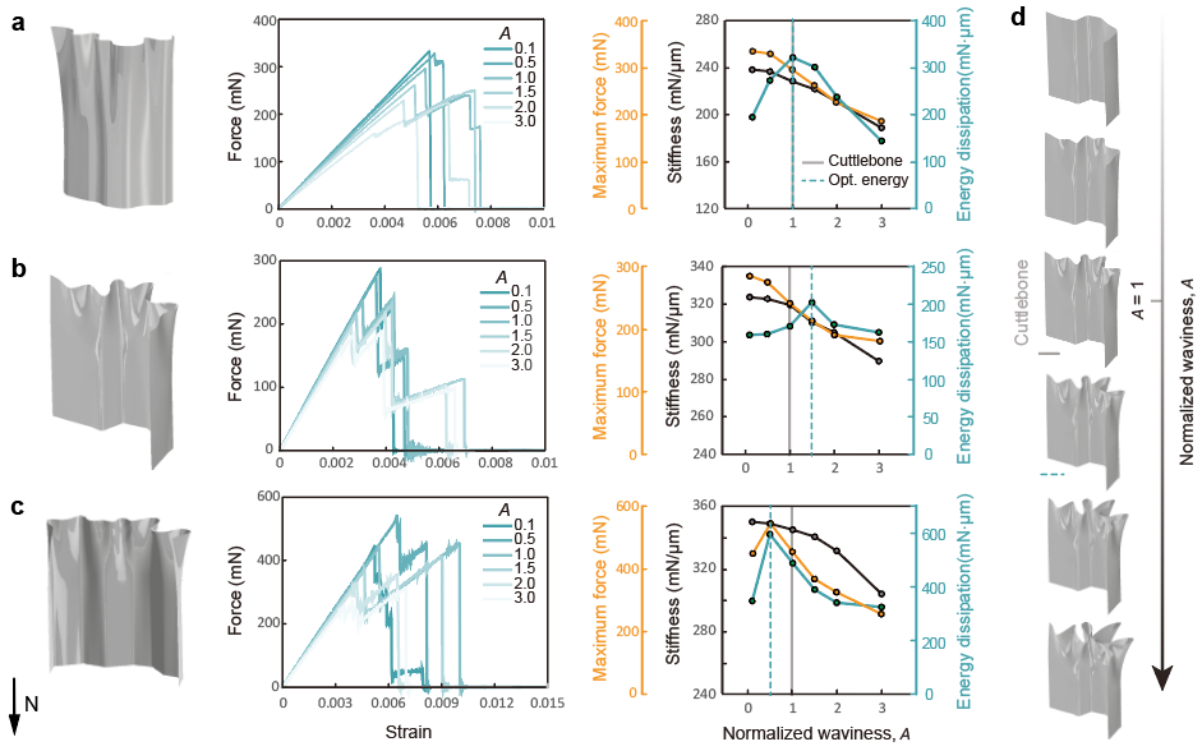

Fig. 4. Mechanics of single walls with controlled variation of waviness: there exists optimal waviness amplitudes of maximum energy absorption. (**a-c**) Effect of waviness amplitude, *A*, on the stiffness, strength, and energy dissipation of three single walls with control variation of waviness. (**d**) Schematics showing the generated walls with different waviness, controlled by parameter *A*. *A* = 1 corresponds to the original walls reconstructed based on the CT data.

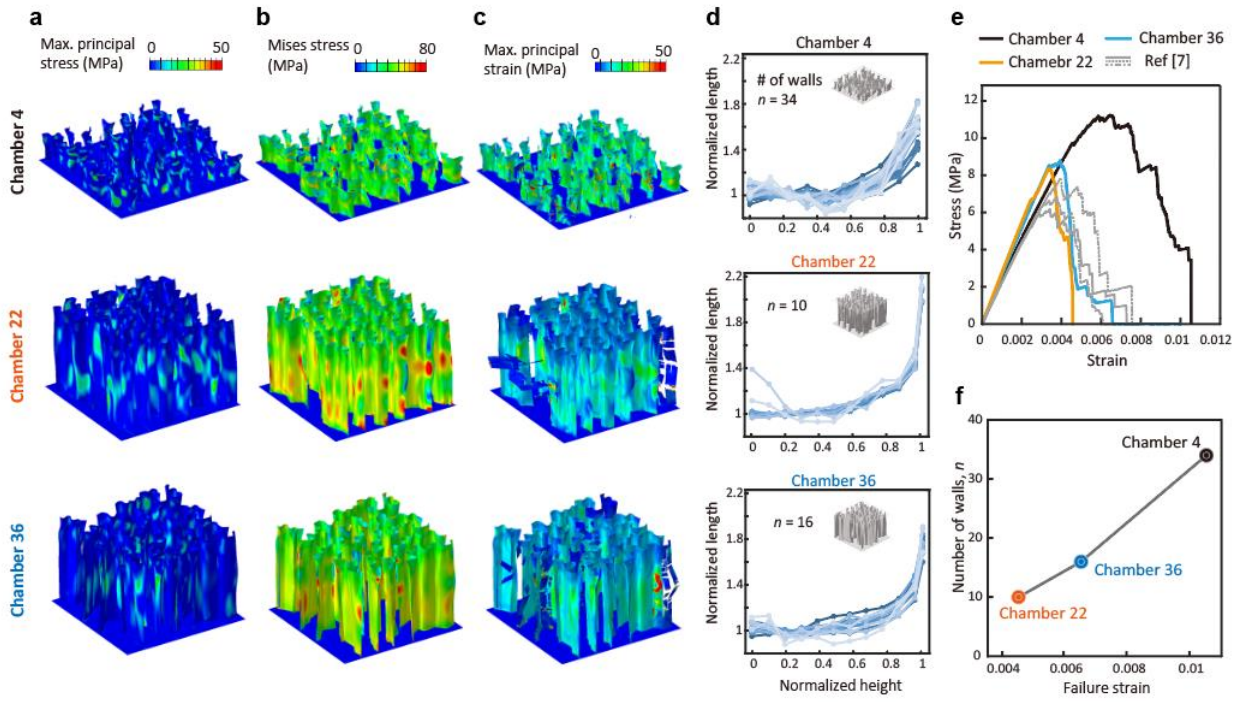

Fig. 5. Stress distribution and fracture initiation of three chambers under vertical compression. (**a**) and (**b**) show the maximum principal stress and Mises stress distribution at applied compressive strains of 0.001. (**c**) shows the maximum principal strain at the fracture initiation. The three columns are for chamber 4, 22, and 36, respectively. (**d**) Profile of the walls in each chamber. *n* is the number of the identified walls. (**e**) A comparison of the stress-strain curves of the three selected chambers to results of reference [7]. (**f**) Correlation between failure strains of the chambers and the number of walls in the chamber.

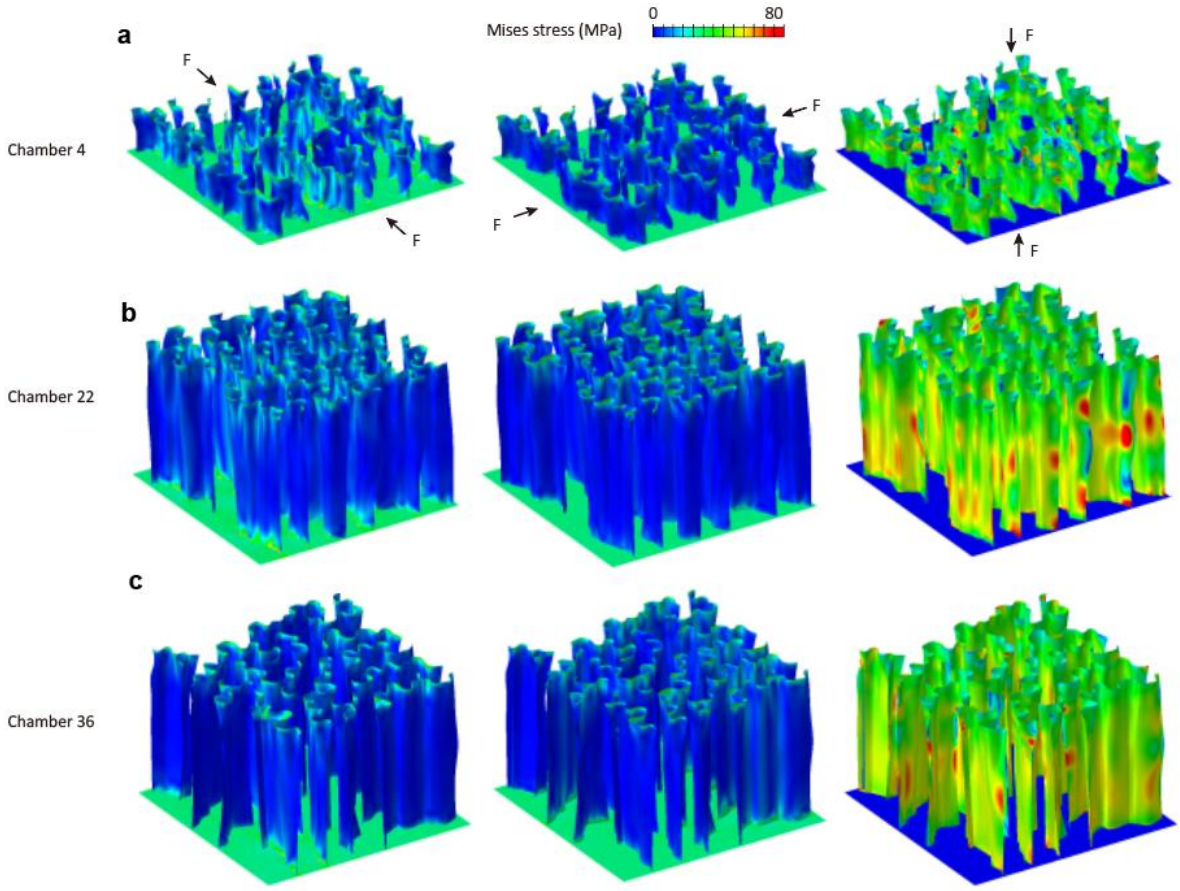

Fig. 6. Stress distribution of three chambers in three different directions of loading, "F". The Mises stress due to loading in the x, y, and z directions, for (**a**) chamber 4, (**b**) chamber 22, and (**c**) chamber 36.

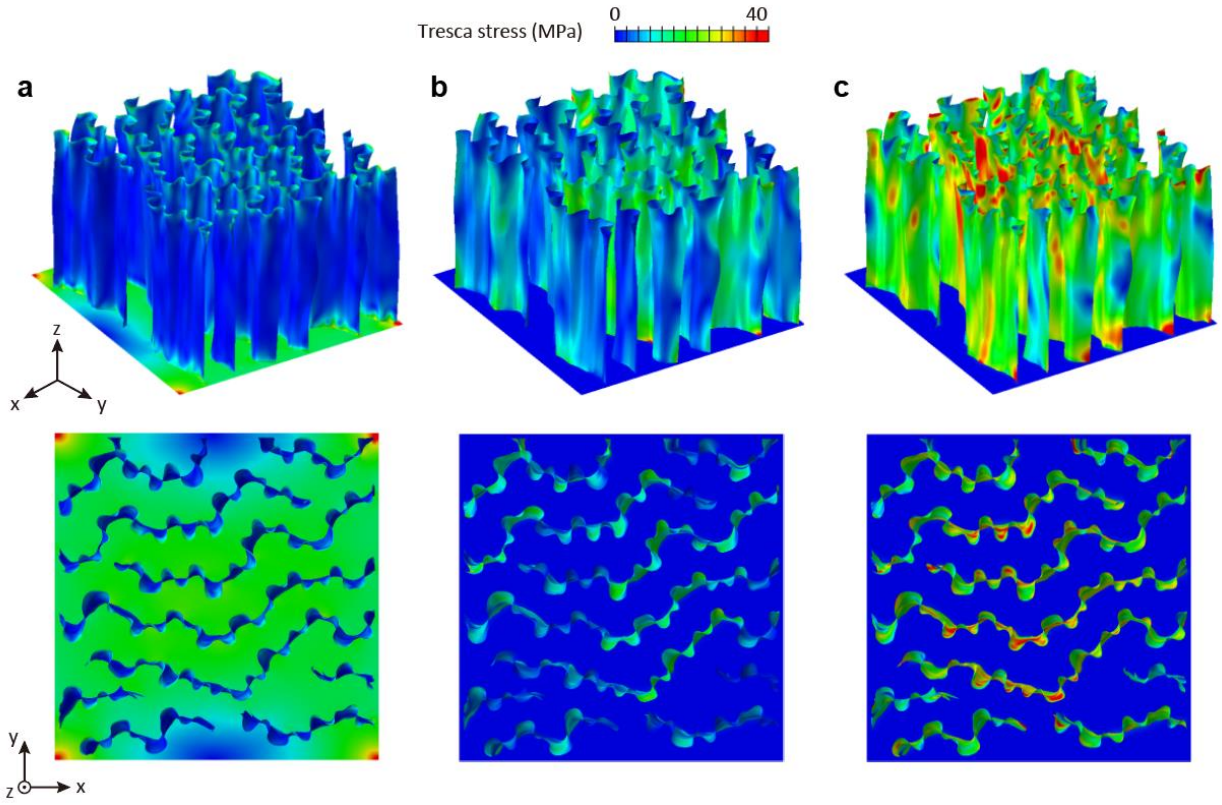

Fig. 7. Stress distribution of chamber 22 under shear in the (**a**) xy plane, (**b**) yz plane, and (**c**) zx plane.

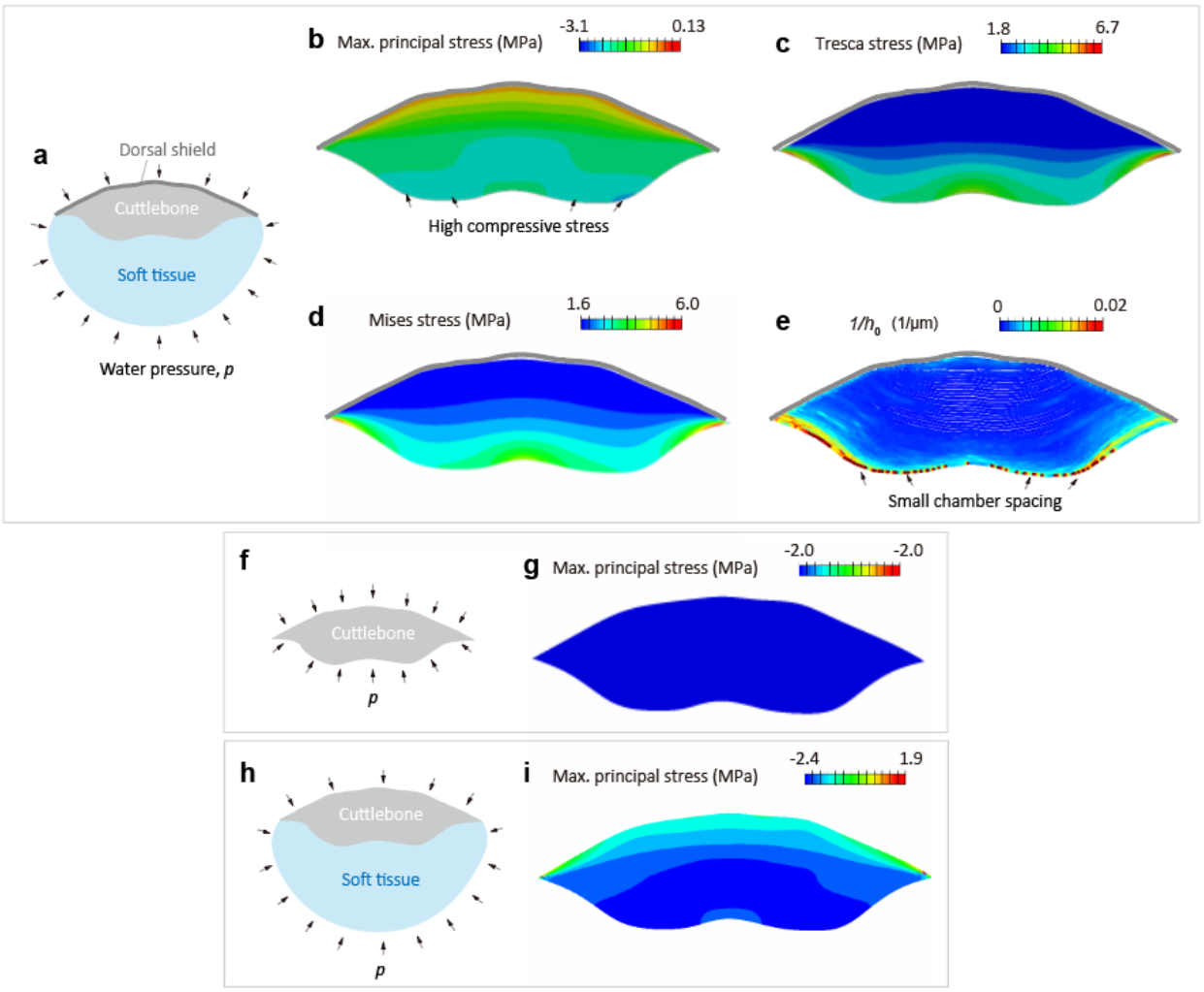

Fig. 8. Stress distribution at the cross-section of the cuttlebone. The simulation setup for the entire cuttlebone on the structural level is shown in (**a**) with dorsal shield on the top and soft tissue underneath the cuttlebone. (**b**) Distribution of maximum principal stress, (**c**) Tresca stress, and (**d**) Mises stress on the cross-section of the cuttlebone. (**e**) The distribution of inversed chamber spacing ($1/h_0$) on the cross-section of the cuttlebone. (**f**) The cuttlebone-only model with stress distribution shown in (**g**). (**i**) The cuttlebone with soft tissue but without dorsal shield model with stress distribution shown in (h). The soft tissue represents the main body of the cuttlefish which is attached to the bottom edge of the cuttlebone in the model. There is an applied pressure p = 2.03 MPa, equivalent to 200 m depth underwater.

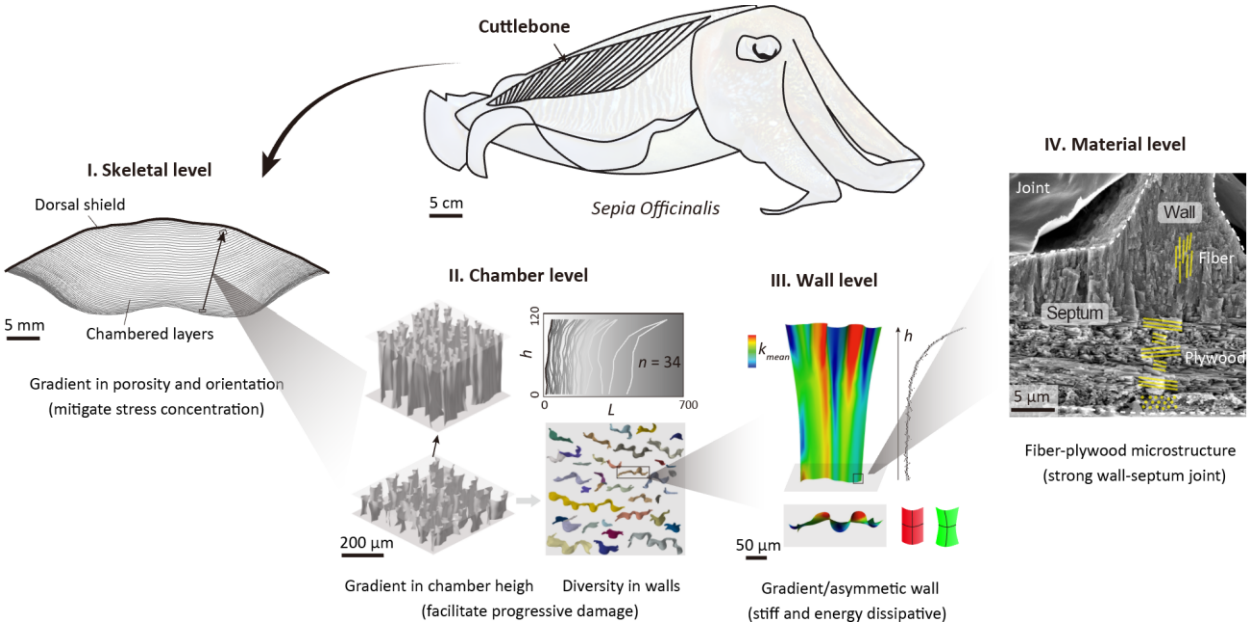

Fig. 9. A summary of the multiscale mechanical design of cuttlebone at the skeletal, chamber, wall, and material level.